RESEARCH ARTICLE

Moisture-radiative cooling instability

Tom Beucler[1] and Timothy W. Cronin[1]

[1]Program in Atmospheres, Oceans and Climate, Massachusetts Institute of Technology, Cambridge, Massachusetts, USA

Abstract Radiative-convective equilibrium (RCE)—the statistical equilibrium state of the atmosphere where convection and radiation interact in the absence of lateral transport—is widely used as a basic-state model of the tropical atmosphere. The possibility that RCE may be unstable to development of large-scale circulation has been raised by recent modeling, theoretical, and observational studies, and could have profound consequences for our understanding of tropical meteorology and climate. Here, we study the interaction between moisture and radiative cooling as a contributor to instability of RCE. We focus on whether the total atmospheric radiative cooling decreases with column water vapor; this condition, which we call moisture-radiative cooling instability (MRCI), provides the potential for unstable growth of moist or dry perturbations. Analytic solutions to the gray-gas radiative transfer equations show that MRCI is satisfied when the total column optical depth—linked to column water vapor—exceeds a critical threshold. Both the threshold and the growth rate of the instability depend strongly on the shape of the water vapor perturbation. Calculations with a realistic radiative transfer model confirm the existence of MRCI for typical tropical values of column water vapor, but show even stronger dependence on the vertical structure of water vapor perturbation. Finally, we analyze the sensitivity of atmospheric radiative cooling to variability in column water vapor in observed tropical soundings. We find that clear-sky MRCI is satisfied across a range of locations and seasons in the real tropical atmosphere, with a partial growth rate of $\sim$1 month.

1. Introduction

Spatial and temporal variability of water vapor in the tropical atmosphere play a large role in Earth's energy balance—due not only to the direct effects of water vapor as a greenhouse gas, but also to the role of humidity in modulating clouds. This variability is usually understood as a result from heterogeneous external forcing—including spatial variability in incident sunlight, sea surface temperature and ocean heat uptake, the distribution of land, and transport of air from higher latitudes. However, moisture variability may also result from internal instabilities of the tropical atmosphere to moist or dry perturbations, which can grow from a homogeneous basic state. If internal instability leads to much of the variability of humidity in the tropics, it could have significant consequences for our understanding of intraseasonal disturbances in the tropical atmosphere (e.g., the Madden-Julian oscillations and tropical cyclones), as well as longer-term variations in Earth's energy balance (e.g., climate change). This paper is centered on the idea that radiative-convective equilibrium (RCE), a classical basic state for the tropical atmosphere, may allow for unstable interaction between water vapor and radiative cooling. If unchecked by other influences, these interactions lead to the growth of dry and moist perturbations.

The starting point for this idea is the existence of a basic state for the tropical atmosphere: radiative-convective equilibrium (RCE). RCE is the hypothetical equilibrium (in a statistical sense) of the atmosphere when radiation, convection, and water phase changes are taken into account, and in the absence of lateral transport. RCE has been widely used to study the controls on global-mean temperature, and was foundational in our early understanding of climate sensitivity [*Ramanathan and Coakley*, 1978; *Manabe and Strickler*, 1964]. It is accepted that RCE is uniquely defined when the greenhouse gases and clouds are held fixed [e.g., *Emanuel*, 1994], but one can ask: is RCE unstable to small perturbations, with fixed insolation and surface temperature, but allowing greenhouse gases to vary?

The first affirmative answer to this question was provided by *Held et al.* [1993], who showed that atmospheric convection could spontaneously organize into a small moist cluster with mean ascent, surrounded by a dry subsiding area. Since then, this unstable behavior has been referred to as the self-aggregation of

convection. Its mechanisms have been studied in 3D cloud-resolving models [*Tompkins*, 2001; *Jeevanjee and Romps*, 2013; *Wing and Emanuel*, 2014; *Muller and Bony*, 2015; *Holloway and Woolnough*, 2016; *Bretherton et al.*, 2005] and general circulation models [*Coppin and Bony*, 2015]; on an *f*-plane, where it systematically leads to cyclogenesis [*Bretherton and Khairoutdinov*, 2015; *Nolan et al.*, 2007; *Khairoutdinov and Emanuel*, 2013], as well as on a β-plane, where it can generate Madden-Julian Oscillation-like disturbances [*Arnold and Randall*, 2015]. The weak temperature gradient (WTG) framework [*Sobel et al.*, 2001] has proven useful to isolate this instability and study the possibility of multiple radiative-convective equillibria [*Sessions et al.*, 2010, 2015], especially in a single column [*Sobel et al.*, 2007; *Emanuel et al.*, 2014], where the effects of large-scale circulation are included by allowing large-scale vertical velocities to moisten or dry the column by vertical advection. *Emanuel et al.* [2014] made fundamental progress by showing the instability of a two-layer atmosphere to coupled lower and upper tropospheric water vapor perturbations in the limit of high surface temperature. However, layered models are highly parameterized and only give valid expressions for radiative fluxes in the optically thin limit—in contradiction of the high surface temperature limit. Moreover, the two-layer instability criterion cannot easily be applied to observations and model outputs, which are much more highly resolved in the vertical. Consequently, we still lack a simple theory that explains when instability of RCE may occur.

This paper poses a simple yet general criterion: if the total atmospheric radiative cooling decreases when column water vapor increases, then RCE may be unstable to growth of moist or dry perturbations. We denote this condition—of decreasing column atmospheric cooling with increasing column water vapor—as "moisture-radiative cooling instability," or MRCI for short (section 2.1). MRCI is neither a necessary nor a sufficient condition for actual growth of moist and dry perturbations, because real perturbations may be amplified or damped by other processes, such as surface fluxes, moisture-convection interactions, and dynamical export or import of moist static energy. But we believe that MRCI is a useful condition to study and describe because it is amenable to theoretical, model, and observational analysis, and because it can be expressed as a partial growth rate of moisture perturbations in the absence of other influences.

Starting from fundamental principles of radiative transfer, we show that MRCI is likely above a critical column water vapor value. Both the critical threshold as well as the growth rate, however, depend on the vertical structure of the moisture perturbation. We build a physical understanding of MRCI by starting from the clear-sky longwave radiation feedback in a gray atmosphere (section 2.2), and progressively adding clear-sky shortwave heating (section 2.3) and longwave cloud-radiation interactions (section 2.4). Using the rapid radiative transfer model (RRTMG), we then relax the gray approximation and show that MRCI can also be satisfied when using real-gas radiation, but the minimum column water vapor required for MRCI can be more sensitive to the vertical structure of the moisture perturbation than with gray-gas radiation (section 3). Finally, we combine observed atmospheric soundings with the RRTMG to show that environmental variability of water vapor in the real tropics frequently leads to clear-sky MRCI, across a range of geographic locations and seasons (section 4).

2. Theory

2.1. Moisture-Radiative Cooling Instability
Starting from an equilibrium basic state, a positive column water vapor perturbation may amplify if it induces large-scale ascending motion, converging additional moisture into the column. In this section, we derive a simple evolution equation (6) for the perturbation atmospheric column water vapor content (in kg m^{-2}), based on coupling between the column radiative heating perturbation and the large-scale convergence or divergence of water vapor.

The column water vapor, $\widehat{r}$, can be defined hydrostatically from the water vapor mixing ratio r (ratio of water vapor to dry air densities):

$$\widehat{r} \stackrel{\text{def}}{=} \int_0^{p_s} r(p) \frac{dp}{g}, \tag{1}$$

where we have introduced the atmospheric pressure p, its value p_s at the surface, and the gravity constant g. Here and elsewhere we use an overhat $\widehat{}$ to indicate a density-weighted column integral. To examine the stability of a small water vapor perturbation $\widehat{r}'$, we adopt an energetic perspective, and introduce the column moist static energy $\widehat{MSE}$, defined as:

$$\widehat{MSE} \overset{def}{=} \underbrace{L_v \widehat{r}}_{\text{Latent heat}} + \underbrace{c_p \widehat{T}}_{\text{Internal heat}} + \underbrace{\widehat{\phi}}_{\text{Potential energy}}, \tag{2}$$

and approximately conserved by an individual air parcel during moist adiabatic processes [*Arakawa and Schubert*, 1974]. L_v is the latent heat of vaporization of water, c_p the specific heat capacity at constant pressure, $\widehat{T}$ the column-integrated absolute temperature and $\widehat{\phi}$ the column geopotential. In the Tropics, the Coriolis force is too weak to sustain horizontal pressure and temperature gradients: the weak temperature gradient approximation [*Sobel et al.*, 2001] holds reasonably well, and we can approximate $\widehat{T}$ and $\widehat{\phi}$ as climatologically fixed. Variations of column-integrated moist static energy are thus given to first order by the latent heat variations, $L_v\widehat{r}'$. In the troposphere, the only contributors to the column moist static energy budget are the total surface enthalpy flux F_s, the total atmospheric radiative cooling rate $\widehat{Q}$ (units W m^{-2}) and the advection of moist static energy [e.g., *Neelin and Held*, 1987]. The radiative cooling $\widehat{Q}$ is defined as positive for atmospheric cooling, and is a sum of longwave ($\widehat{Q}_L$) and shortwave ($-\widehat{Q}_S$) components.

To greatly simplify our derivation, and focus on the role of radiative heating anomalies, we set the $\widehat{MSE}$ advection to zero, yielding:

$$\frac{\partial \widehat{MSE}}{\partial t} \approx L_v \frac{\partial \widehat{r}}{\partial t} = F_s - \widehat{Q}. \tag{3}$$

Neglecting $\widehat{MSE}$ advection corresponds to an assumption of zero gross moist stability—that convergence of dry static energy exactly balances divergence of latent heat (or vice-versa) [*Yu et al.*, 1998; *Inoue and Back*, 2015b]. This assumption is artificial, especially on daily timescales, where the $\widehat{MSE}$ advection has been shown to be the primary driver of $\widehat{MSE}$ recharge/discharge [*Inoue and Back*, 2015a]. However, on longer time scales (weekly/monthly), the diabatic terms F_s and $\widehat{Q}$ become of larger importance, and a tropical atmospheric column may be unstable without up-gradient MSE transport. In that spirit, RCE (denoted by overlines from now on) is an appropriate basic state for the column, since it represents a balance between the surface turbulent fluxes and radiative cooling in the absence of $\widehat{MSE}$ advection:

$$\overline{F_s} \overset{def}{=} \overline{\widehat{Q}}. \tag{4}$$

To isolate the role of radiation-water vapor interaction, we fix the surface temperature and assume that the surface flux F_s stays equal to its RCE value $\overline{F_s}$ at all times. We denote the perturbations from RCE by primes. Linearizing the evolution equation (3) about RCE, where the balance (4) holds, leads to a simple evolution equation for the column water vapor perturbation $\widehat{r}'$ to first order:

$$L_v \frac{\partial \widehat{r}'}{\partial t} = -\overline{\frac{\partial \widehat{Q}}{\partial \widehat{r}}} \widehat{r}' + O\left[(\widehat{r}')^2\right]. \tag{5}$$

From equation (5), we can compute the evolution of an initial perturbation in time:

$$\widehat{r}'(t) = \widehat{r}'(t=0) \exp(\lambda t) \tag{6}$$

$$\lambda = \underbrace{-\frac{1}{L_v} \overline{\frac{\partial \widehat{Q}}{\partial \widehat{r}}}}_{\text{Decay/Growth rate}}, \tag{7}$$

from which we obtain a potential linear instability criterion for moisture-radiative cooling instability (MRCI), with growth rate λ. An initial dry or moist perturbation may amplify if atmospheric radiative cooling decreases with column water vapor ($\lambda = -\partial\widehat{Q}/\partial\widehat{r} > 0$). The simple mechanism of this instability is illustrated in Figure 1. Note that vertical advection of MSE could be computed self-consistently within the weak temperature gradient framework, assuming that perturbation convective enthalpy fluxes are zero and that the vertical structure of perturbation radiative heating drives vertical velocities. Such a computation amounts to calculating the combined radiative and vertical-advective perturbations in the moist static energy budget. To isolate the contribution of radiative processes, we focus only on the radiative term in this paper, although preliminary results suggest that vertical MSE advection may substantially amplify the MRCI growth rates. The following sections aim to compute $\widehat{Q}(\widehat{r})$ in simple but general cases, to show when and why the MRCI condition can be satisfied.
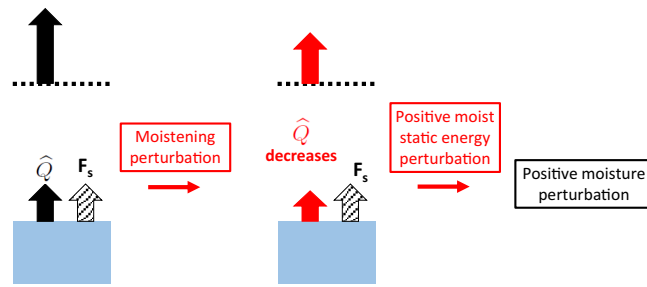
Figure 1. Mechanism of MRCI: A moist perturbation decreases the radiative cooling, leading to an amplification of this moist perturbation.

2.2. Clear-Sky Longwave Radiation
2.2.1. Temperature and Mixing Ratio Profiles

Understanding infrared radiative transfer in the atmosphere requires knowledge of the vertical structure of temperature and greenhouse gases. We will use simple analytical expressions to model Tropical temperature and water vapor profiles [e.g., *Robinson and Catling*, 2012; *Weaver and Ramanathan*, 1995], informed by bi-daily profiles from Chuuk Lagoon (Federated States of Micronesia, station 91334 PTKK), in January and over the past 20 years (January 1996/1997/. . ./2016; the data are retrieved from the University of Wyoming archive, at www.weather.uwyo.edu/upperair/sounding.html). The average temperature profile $T(p)$ and water vapor profile $r(p)$ are depicted in Figure 2.

We fit the mixing ratio profile by assuming a simple power law of the form:

$$r(p) = r_s \left(\frac{p}{p_s}\right)^n,$$ (8)

where r_s is the surface mixing ratio and n is the ratio of the pressure to the water vapor scale heights. For Chuuk Lagoon, $n \approx 3$ is a reasonable choice for this ratio, and we will use it as our reference value from now on. Note that the power law does not always capture the shape of the water vapor profile in the mid- and upper troposphere, especially when the atmospheric moisture content varies (this misfit can be seen above 300 hPa in Figure 2c). Furthermore, $n = 3$ is not the best fit for all tropical locations (it varies from ~ 2 to 4). We also seek a simple power law fit for the temperature profile:

$$T = T_s \left(\frac{p}{p_s}\right)^{\frac{\Gamma_m R_d}{g}},$$ (9)

where T_s is the surface temperature, R_d the specific gas constant of dry air and Γ_m is a representative average lapse rate (6.3 K km^{-1} in Figure 2a). Equation (9) can be interpreted as an all-troposphere profile with Γ_m given by the self-consistent moist adiabatic lapse rate at 500 hPa for a prescribed value of T_s. Deviations from the observed temperature profile in Figure 2a are less than 5 K below 200 hPa, but become much larger in the stratosphere—equation (9) predicts continued decrease in T with height, but shortwave absorption
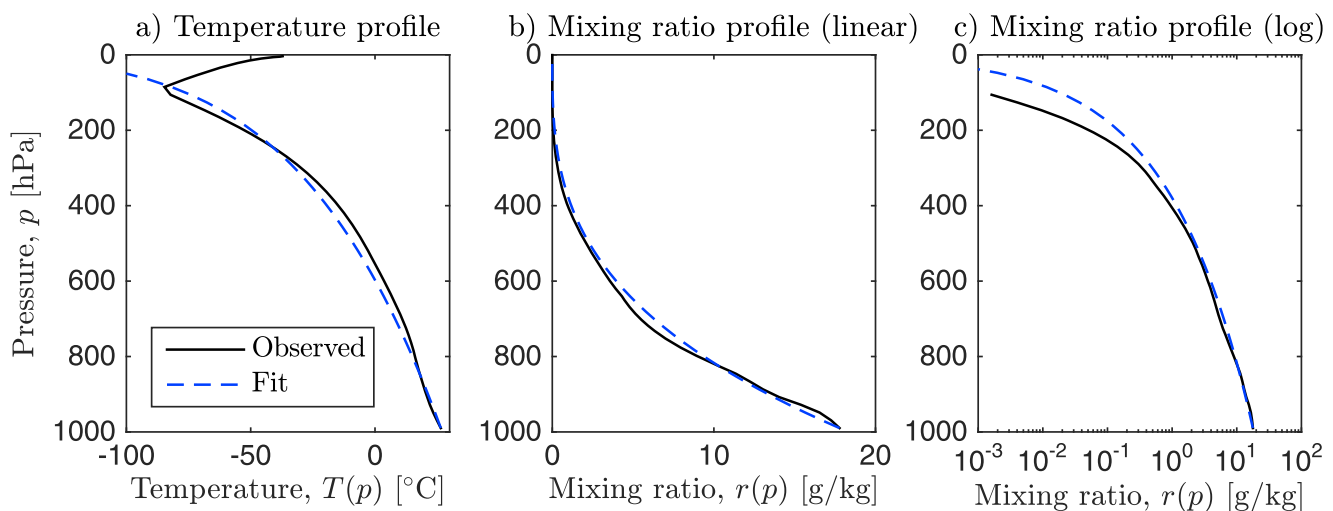

Figure 2. (a) Temperature profile $T(p)$ and (b, c) water vapor mixing ratio profile $r(p)$ in January at Chuuk Lagoon. The average observational profiles are shown in solid black lines and the idealized fits are shown in blue dashed lines; Figures 2b and 2c are identical but Figure 2b has a linear scale for $r(p)$ and c) has a logarithmic scale.

causes the temperature in the real atmosphere to increase with height. We will use these simple power laws for the temperature and mixing ratio profiles, together with gray radiative transfer equations, as a starting point to explore MRCI.

2.2.2. Theoretical Framework

We first focus on the clear-sky longwave radiation, which constitutes the bulk of the atmospheric cooling. Following *Robinson and Catling* [2012] and *Takahashi* [2009], we make several assumptions which allow us to obtain an analytical expression for $\widehat{Q}_L(\hat{r})$. First, we consider a one-dimensional, plane-parallel atmosphere, and use the two-stream Schwarzschild equations [e.g., *Chandrasekhar*, 1960] for the upwelling and downwelling radiative fluxes (respectively $\mathcal{F}_\uparrow$ and $\mathcal{F}_\downarrow$):

$$\frac{d\mathcal{F}_\uparrow}{d\tau} = \mathcal{F}_\uparrow - \sigma T^4, \tag{10}$$

$$\frac{d\mathcal{F}_\downarrow}{d\tau} = -(\mathcal{F}_\downarrow - \sigma T^4). \tag{11}$$

σ is the Stefan-Boltzmann constant, T the atmospheric temperature profile and τ the optical thickness. We assume that water vapor is the only absorbing gas in the longwave, and we make the gray approximation [e.g., *Liou*, 2002] with an average absorption coefficient $k_{LW} \approx 0.1$ m^2 kg^{-1}. The neglect of other greenhouse gases, the gray approximation, and the precise choice of k_{LW} are all significant assumptions, and we emphasize that this derivation is done for illustrative rather than exact purposes. We can then relate the differential optical thickness $d\tau$ to the differential pressure dp, accounting for pressure broadening of water vapor absorption strength by scaling the differential optical thickness by p/p_s:

$$d\tau = Dk_{LW}r(p)\frac{p}{p_s}\frac{dp}{g}. \tag{12}$$

Here, we have introduced a diffusivity factor $D = 5/3$ into the optical thickness itself, to account for the integration of the radiances over a hemisphere [*Armstrong*, 1968; *Rodgers and Walshaw*, 1966]. By combining equations (12), (8) and (9), it is possible to express:

1. The temperature as a function of the optical thickness:

$$T = T_s\left(\frac{\tau}{\tau_s}\right)^{\alpha/4} \quad \text{where } \alpha \stackrel{\text{def}}{=} \frac{4\Gamma_m R_d}{(n+2)g}, \tag{13}$$

2. The total optical thickness of the atmosphere as a function of the profile properties:

$$\tau_s \stackrel{\text{def}}{=} \tau(p=p_s) = \frac{Dk_{LW}p_s r_s}{(n+2)g}. \tag{14}$$

We can obtain the surface net longwave flux SLW, the outgoing longwave radiation OLR, and thus the atmospheric radiative cooling $\widehat{Q}_L$ by integrating equations (10) and (11). Assuming that the surface radiates like a black-body of temperature T_s and that there is no incoming longwave radiation at the top of the atmosphere yields:

$$\frac{\text{SLW}}{\sigma T_s^4} \stackrel{\text{def}}{=} \frac{\mathcal{F}_\uparrow(\tau_s) - \mathcal{F}_\downarrow(\tau_s)}{\sigma T_s^4} = \underbrace{1}_{\text{Surface}\to\text{Atmosphere}} - \underbrace{\int_0^{\tau_s} d\tau'\left(\frac{\tau'}{\tau_s}\right)^\alpha e^{-(\tau_s-\tau')}}_{\text{Atmosphere}\to\text{Surface}}, \tag{15}$$

$$\frac{\text{OLR}}{\sigma T_s^4} \stackrel{\text{def}}{=} \frac{\mathcal{F}_\uparrow(0) - \mathcal{F}_\downarrow(0)}{\sigma T_s^4} = \underbrace{e^{-\tau_s}}_{\text{Surface}\to\text{Space}} + \underbrace{\int_0^{\tau_s} d\tau'\left(\frac{\tau'}{\tau_s}\right)^\alpha e^{-\tau'}}_{\text{Atmosphere}\to\text{Space}}, \tag{16}$$

$$\frac{\widehat{Q}_L}{\sigma T_s^4} \stackrel{\text{def}}{=} \frac{\text{OLR}-\text{SLW}}{\sigma T_s^4} = e^{-\tau_s} - 1 + \int_0^{\tau_s} d\tau'\left(\frac{\tau'}{\tau_s}\right)^\alpha\left(e^{-(\tau_s-\tau')} + e^{-\tau'}\right). \tag{17}$$

We derive these analytical forms of the radiative fluxes in Appendix A. The net SLW (15) is the blackbody emission from the surface (T_s), minus the total atmospheric downward emission at the surface, which increases with the temperature exponent α defined by equation (13). The OLR (16) is the sum of the surface

blackbody emission that has not been absorbed by the atmosphere, and the total atmospheric upward longwave emission at the top of the atmosphere. Finally, the longwave radiative cooling $\widehat{Q}_L$ (17) is the difference between the OLR and the SLW (difference between the top and bottom arrows on Figure 1). In order to examine $\widehat{Q}_L$ as a function of $\widehat{r}$, and thus determine whether clear-sky longwave MRCI is satisfied, we also need to relate the column water vapor to the characteristics of the sounding. This can be done by combining equations (1) and (8):

$$\widehat{r} = \frac{r_s p_s}{(n+1)g}. \tag{18}$$

2.2.3. Clear-Sky Longwave MRCI

We can use the results of section 2.1 to evaluate the sensitivity of the longwave atmospheric radiative cooling (17) to column water vapor. Because the water vapor mixing ratio decreases with height, we expect the radiative cooling to change less if we remove water vapor near the surface, where the atmosphere is more optically thick, than near the top of the atmosphere. Thus, we choose two simple ways of adding or removing water vapor to the column, which are both illustrated in Figure 3:

1. We fix the shape of the water vapor mixing ratio profile (n), but vary its surface value r_s. Water vapor is thus mostly added or removed in the lower troposphere.
2. We fix the surface mixing ratio (r_s) but vary its shape n. Water vapor is thus mainly added or removed in the midtroposphere.

These variations in column water vapor can be thought of as a representation both of different RCE states about which a linear stability analysis applies, and as large-amplitude perturbations to the water vapor profile from a given RCE state. Variability of water vapor profiles in the real world is complex, and generally includes both of these idealized behaviors. We will later show, however, that water vapor variability in the Tropics looks more like b) the case of varied shape with fixed surface mixing ratio—so the right-hand plots of subsequent Figures should be treated as more realistic.

Looking at the contribution of the surface net longwave flux (SLW) and the outgoing longwave radiation (OLR) in Figure 4 gives a first understanding of the MRCI physical mechanism:

1. Without water vapor ($\widehat{r}=0$), the surface directly radiates to space, and the atmospheric radiative cooling is zero. The OLR and the SLW are both at their maximal values.
2. For small water vapor content, the SLW falls sharply as the boundary layer becomes opaque, and the atmosphere emits almost as much longwave radiation to the surface as it receives from the surface. For higher water vapor content, the SLW decays to zero.
3. The OLR decreases much more slowly with water vapor, consistently with the observational and modeling literature [e.g., *Allan and Soden*, 2008; *Harrop and Hartmann*, 2015]. The OLR can be thought of as
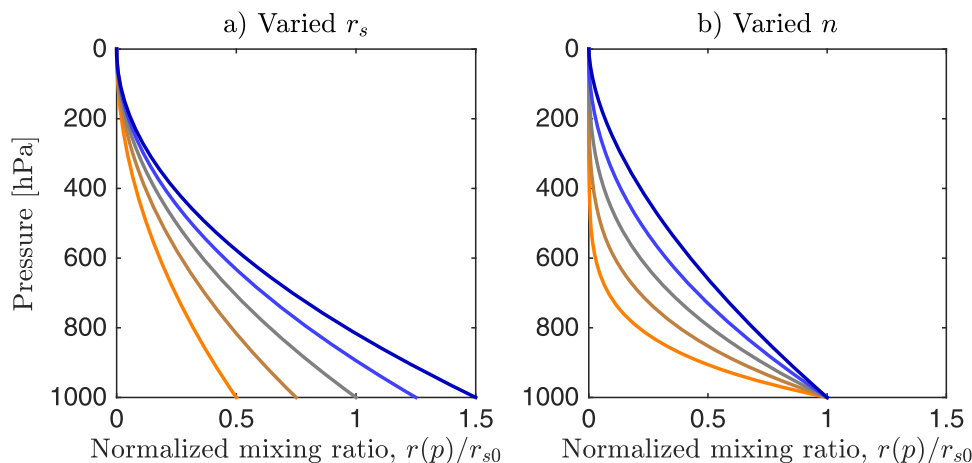

Figure 3. Two methods of varying column water vapor used in this paper; (a) varied mixing ratio (r_s) and fixed shape; (b) varied shape ($n = 1.7, 2.2, 3.0, 4.3, 7.0$) and fixed surface mixing ratio. The reference profile is gray and the different colors represent equal increments of total column water vapor.
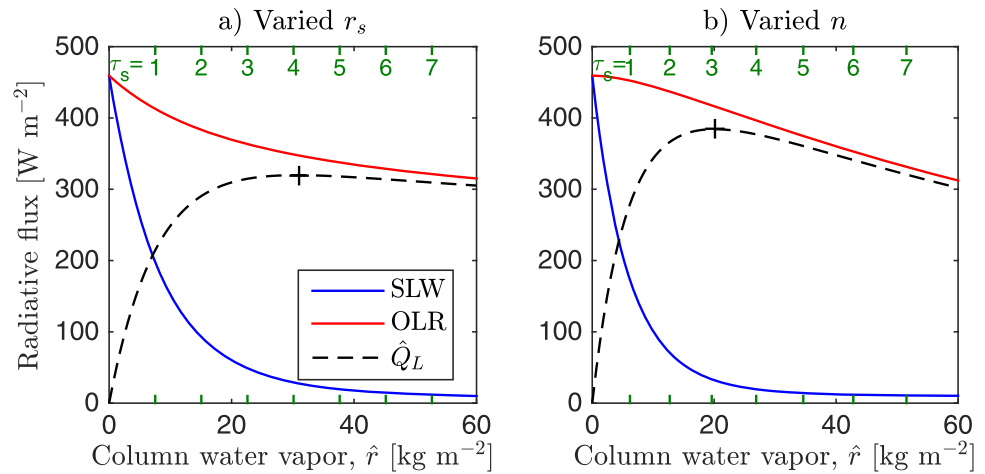
Figure 4. Outgoing longwave radiation (OLR), surface net longwave radiation (SLW), and longwave clear-sky radiative cooling $\widehat{Q}_L$ as a function of column water vapor $\hat{r}$, (a) varying the surface mixing ratio at fixed shape, and (b) varying the water vapor profile shape at constant surface mixing ratio. Crosses show maxima of radiative cooling, and green axis labels indicate surface optical thickness, τ_s. The surface temperature is 300K. Note the similarity to figure 4 of *Takahashi* [2009].

scaling with the fourth power of the effective upward emission temperature, which decreases slowly as the atmosphere becomes optically thicker and the emission level moves upward.

4. Consequently, for small water vapor content, the atmospheric radiative cooling increases with water vapor, whereas it decreases with water vapor for higher water vapor content. Thus, for gray-gas radiation, there is a critical water vapor threshold $\widehat{r}_{crit}$, above which MRCI is satisfied.

Figure 4 allows us to obtain the critical threshold $\widehat{r}_{crit}$ from the abscissa of the maximum (marked with crosses), and the growth rate from the slope of the curve $\widehat{Q}_L(\widehat{r})$. Comparing the two presented cases shows that MRCI:

1. Is satisfied above a smaller critical threshold $\widehat{r}_{crit}$ at varied shape n than at varied surface mixing ratio r_s.
2. Has strongest growth rates for varied shape n (typical value of 1/15 days), much larger than those at varied surface mixing ratio r_s (typical value of 1/60 days). The reader is referred to Appendix D for the exact calculation of the growth rate in both cases.

These findings confirm that the atmosphere is more unstable to addition or removal of water vapor in the mid and upper troposphere than in the lower troposphere. The typical growth rates found for the MRCI at varied n are consistent with the numerical findings of *Wing and Emanuel* [2014], where the water vapor content mostly varied in the mid and upper troposphere. Since the water vapor content in RCE scales exponentially with surface temperature, we can also roughly identify a threshold surface temperature above which $\overline{\overline{\widehat{r}}} > \widehat{r}_{crit}$. To make this statement more rigorous, we verify that the functional properties of $\widehat{Q}_L(\widehat{r})$ do not change significantly with surface temperature due to changes in either lapse rate or surface mixing ratio (Appendix B). Note that these results depend on both the gray approximation and the choice of k_{LW}, and we will compare them below with calculations using real-gas radiative transfer (section 3).

2.3. Clear-Sky Shortwave Radiation

Clear-sky shortwave radiation is always a destabilizing factor for moisture perturbations from RCE, regardless of $\widehat{r}$ or the vertical structure of the perturbation. As column water vapor increases, there is more water vapor to absorb shortwave radiation, which decreases the total radiative cooling. To incorporate shortwave radiation in our radiative model, we write the Schwarzschild equation for the downwelling shortwave radiative flux $\mathcal{F}_{\downarrow,\mathrm{SW}}$, assuming that water vapor acts as a simple gray absorber in the shortwave:

$$\frac{d\mathcal{F}_{\downarrow,\mathrm{SW}}}{d\tau} = -\varepsilon \mathcal{F}_{\downarrow,\mathrm{SW}}. \qquad (19)$$

The τ on the left side of equation (19) is the longwave optical thickness, so the parameter ε converts between differential shortwave and longwave optical thickness coordinates:
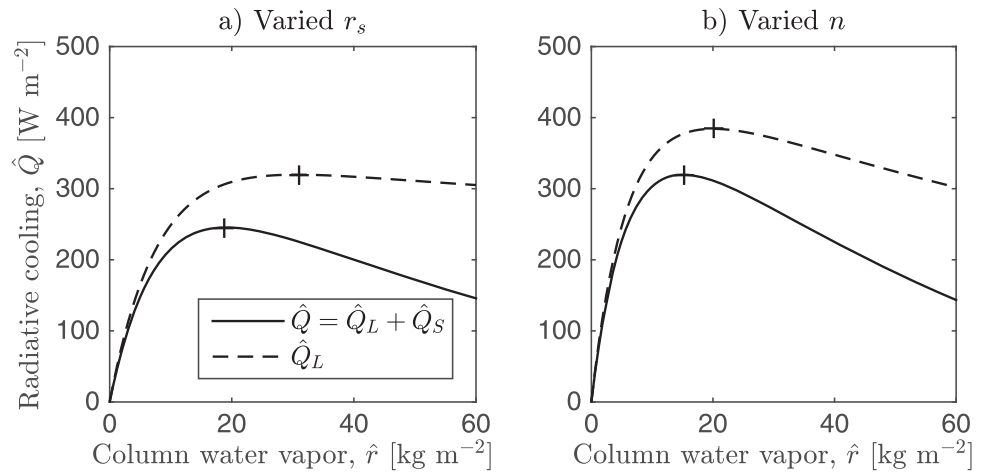
Figure 5. Longwave $\hat{Q}_L$ and total $\hat{Q}$ clear-sky radiative cooling as a function of column water vapor, a) varying the surface mixing ratio at fixed shape, and b) varying the water vapor profile shape at constant surface mixing ratio. Crosses show maxima of radiative cooling. The surface temperature is 300K.

$$\varepsilon = \frac{d\tau_{\text{SW}}}{d\tau_{\text{LW}}} = \frac{k_{\text{SW}}}{k_{\text{LW}}\mu D}. \tag{20}$$

Here, $k_{\text{SW}} \approx 10^{-2}$ m^2 kg^{-1} represents the water vapor absorption coefficient averaged over shortwave frequencies (again chosen for illustrative and not exact purposes), and $\mu = \pi/4$ is the insolation-weighted zenith angle at the equator on the equinox [*Cronin*, 2014]. We integrate equation (19), with time-mean insolation S. The shortwave radiative heating rate $\hat{Q}_S$ is then:

$$\frac{\hat{Q}_S}{S} \overset{\text{def}}{=} \frac{\mathcal{F}_{\downarrow,\text{SW}}(0) - \mathcal{F}_{\downarrow,\text{SW}}(\tau_s)}{S} = 1 - e^{-\varepsilon\tau_s}, \tag{21}$$

which means that the total radiative cooling rate of the atmosphere is $\hat{Q} = \hat{Q}_L - \hat{Q}_S$.

Because ε is a small number, the shortwave heating rate increases slowly with water vapor, contributing further to the MRCI studied in section 2.2, as we can see by the steeper slopes in Figure 5. The typical growth rate of MRCI increases from 1/60 days to 1/12 days for varied r_s, and from 1/15 days to 1/7 days for varied n. The threshold for MRCI, $\hat{r}_{\text{crit}}$, also decreases when shortwave absorption is taken into account (see crosses in Figure 5). Again, these results depend on the gray approximation and the choice of absorption coefficients, and they will be compared below with calculations using real-gas radiative transfer (section 3).

2.4. Cloud Longwave Radiative Effects

Cloud-radiation interaction has been shown to play an important role in self aggregation, and their effects can be stabilizing or destabilizing depending on the characteristics of the cloud cover [*Muller and Bony*, 2015; *Wing and Emanuel*, 2014; *Wing and Cronin*, 2016]. We are especially interested in recent studies that have shown that low thick clouds could be a potential mechanism for MRCI at low surface temperatures [e.g., *Coppin and Bony*, 2015]. After including clear-sky shortwave heating, there was still a threshold $\hat{r}_{\text{crit}}$ below which MRCI was not satisfied. Can this threshold decrease in the presence of clouds? To address this question, we add an idealized cloud in our radiative model. Motivated by the simple idea that the cloud acts as a strong localized absorber and emitter, we approximate it as an infinitesimally thin layer, defined by its optical thickness $\Delta\tau$ and its pressure level p_c. The idealized cloud has no effect on the moist adiabatic temperature profile, but causes a step in the optical thickness profile, which is illustrated in Figure 6.

The atmospheric radiative cooling in the presence of a cloud is computed in Appendix C and given by equation (33). Note that we entirely neglect the shortwave radiative and reflective effects of clouds. To obtain a physical intuition about the cloud radiative effects, it is useful to consider two limits:

1. The limit of a very optically thin cloud ($\Delta\tau \ll \tau_s, 1$). In that case, we recover the clear-sky radiative cooling of sections 2.2 and 2.3: $\hat{Q}_L - \hat{Q}_S$.
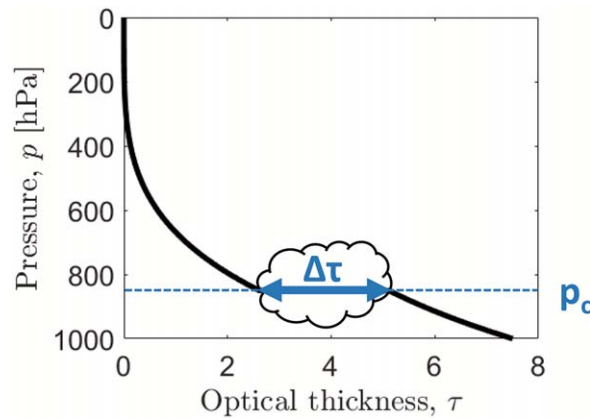
Figure 6. Optical thickness profile for a cloud at p_c=850hPa with cloud optical thickness $\Delta\tau$=2.5.

2. The limit of a very optically thick cloud ($\Delta\tau \gg 1$) in an optically thin clear-sky atmosphere ($\tau_s < 1$). In the absence of shortwave absorption, the atmospheric radiative cooling is then given by:

$$\widehat{Q}_{\Delta\tau\gg1}=\sigma(T_s^4-2T_c^4), \qquad (22)$$

where T_c is the temperature of the cloud. Thus, low clouds (such that $2T_c^4 > T_s^4$) are expected to cool the atmosphere, whereas high clouds (such that $2T_c^4 < T_s^4$) warm the atmosphere.

Figure 7 shows the atmospheric radiative cooling in the presence of four idealized clouds, which differ by their heights (low and high) and their optical thickness (thick and thin). We see that the radiative effects of low clouds are destabilizing, reducing the critical threshold $\widehat{r}_{crit}$ and increasing the MRCI growth rate. Thick low clouds can even reduce $\widehat{r}_{crit}$ to 0. On the other hand, high clouds stabilize the atmosphere by increasing $\widehat{r}_{crit}$ and decreasing the growth rate. Cloud effects generally increase with cloud optical thickness $\Delta\tau$. Note that partial clear sky and partial cloud cover could easily be modeled by a weighted averaging of curves from Figure 7.

The cloud effects we discuss here refer solely to the effect of a static cloud profile on the sensitivity of atmospheric cooling to water vapor. Other stabilizing or destabilizing cloud effects can also occur due to variation of cloud amount or type with column water vapor [e.g., *Harrop and Hartmann*, 2015]. For example, if high cloud amount or optical thickness increases with column water vapor, then $\widehat{Q}$ could decrease with increasing $\widehat{r}$, reinforcing the MRCI growth rate. Such cloud feedbacks have been documented as important in self-aggregation [*Wing and Emanuel*, 2014], but elaborating on them further is beyond the scope of this work.

3. Real-Gas Radiative Transfer

To better understand how the results above depend on the wavelength-dependence of water vapor absorption, we use the RRTMG model [*Iacono et al.*, 2000, 2008; *Mlawer et al.*, 1997] to explore the relationship between column water vapor $\widehat{r}$ and column radiative cooling $\widehat{Q}$ for idealized moisture profiles. We use
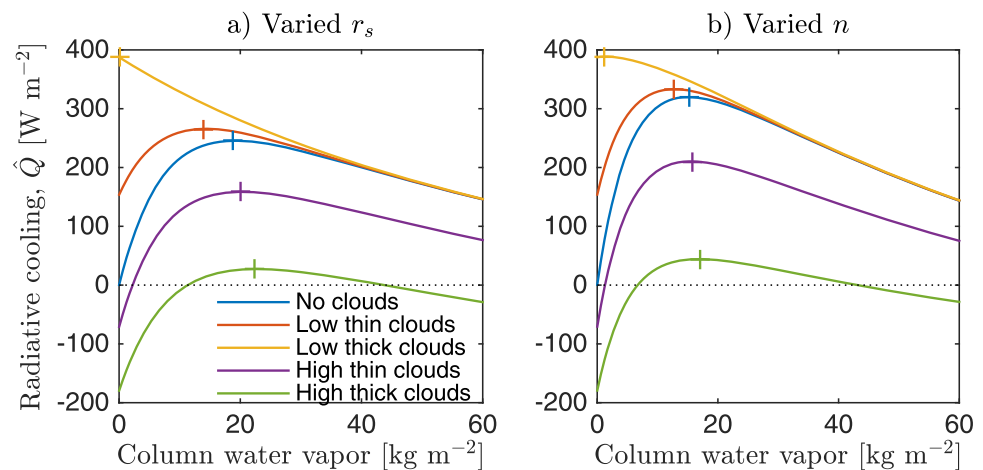

Figure 7. Total radiative cooling in the presence of a low (p_c=900hPa $\Longleftrightarrow$ T_c=295K), high (p_c=200hPa $\Longleftrightarrow$ T_c=234K), thick ($\Delta\tau$=5) or thin ($\Delta\tau$=0.5) cloud with a) varied surface mixing ratio, and b) varied shape. Crosses show maxima of radiative cooling. The surface temperature is 300 K.
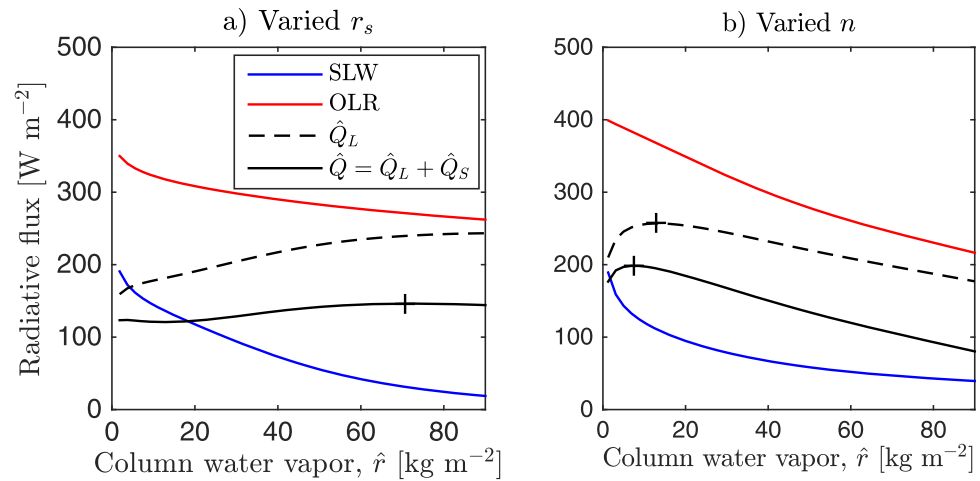
Figure 8. As in Figures 4 and 5, but using the RRTMG model instead of gray-gas radiative transfer. Outgoing longwave radiation (OLR), surface net longwave radiation (SLW), longwave $\widehat{Q}_L$ and total $\widehat{Q}$ clear-sky radiative cooling as a function of column water vapor, (a) varying the surface mixing ratio at fixed shape, and (b) varying the water vapor profile shape at constant surface mixing ratio. Crosses show maxima of radiative cooling. The surface temperature is 300 K.

the version 3.8 of the longwave and shortwave column versions of RRTMG, which is a broadband, two-stream, correlated k-distribution radiative transfer model that has been tested against line-by-line radiative transfer models, and is used in several general circulation models. We use a realistic long-term mean temperature profile from the Chuuk station, together with idealized water vapor profiles given by equation (8). We vary the column water vapor either by varying the surface mixing ratio r_s and holding the pressure scaling exponent n constant, or by varying the pressure scaling exponent n and holding the surface mixing ratio constant. We specify a constant CO_2 mixing ratio of 400 ppmv throughout the depth of the atmosphere, but use no other greenhouse gases.

Clear-sky longwave MRCI is much more sensitive to the vertical structure of water vapor perturbation with real-gas radiation than with gray-gas radiation. There is no longwave instability for varied r_s and $\widehat{r} < 90$ kg m^{-2}, but with fixed r_s, MRCI is satisfied for all $\widehat{r} > 15$ kg m^{-2} (Figure 8). The threshold $\widehat{r}_{crit} \approx 15$ kg m^{-2} for MRCI in the case of varied n is at the very low end of the distribution of $\widehat{r}$ in the real Tropics. Broadly speaking, the shape of the OLR and SLW curves is similar to that in the gray-gas theory, but the net longwave radiation at the surface does not tend toward zero nearly as rapidly with increasing $\widehat{r}$ for real-gas radiative transfer. Values of SLW remain large (~ 50 W m^{-2}) even for moist atmospheres ($\widehat{r} \sim 60$ kg m^{-2}), and allow $d\text{SLW}/d\widehat{r}$ to also be larger in magnitude than in the gray-gas model. Thus, because the instability is determined by the slope of OLR-SLW with $\widehat{r}$, the failure of SLW to rapidly asymptote to zero is the key reason why the real-gas model shows greater sensitivity to the vertical structure of water vapor perturbation. The surface net longwave radiation depends strongly on near-surface specific humidity in the real atmosphere because the optical thickness of water vapor in its least absorbent parts of the spectrum—the water vapor window region of the spectrum from ~ 8 to 12 μm—actually scales with the square of the vapor pressure [e.g., *Cormier et al.*, 2005]. The importance of the atmospheric window for surface longwave cooling motivates a two-band model for the water vapor spectrum, which allows for separate treatment of strongly absorbing and weakly absorbing wavelength ranges. This model of intermediate complexity, presented in Appendix E, gives a much better fit to Figure 8 than is possible for any single choice of k_{LW}, but is still simple enough for the SLW and the OLR to be expressed analytically.

Integrated column shortwave absorption is insensitive to the shape of the moisture perturbation. Including shortwave heating thus increases the instability for the case of varied n, lowering $\widehat{r}_{crit}$ to less than 10 kg m^{-2}, and pushes the case with varied r_s close to neutral stability. The total atmospheric cooling for varied r_s (solid line in Figure 8) actually has more than one local maximum (near 5 and 70 kg m^{-2}). Multiple local maxima in $\widehat{Q}$ can arise with real-gas radiative transfer, because different parts of the thermal spectrum become optically thick at different values of $\widehat{r}$. As a particular spectral region becomes optically thick, it first leads to an increase in atmospheric cooling and then to a decrease (as shown by (17) and $\widehat{Q}_L$ in Figure 4).
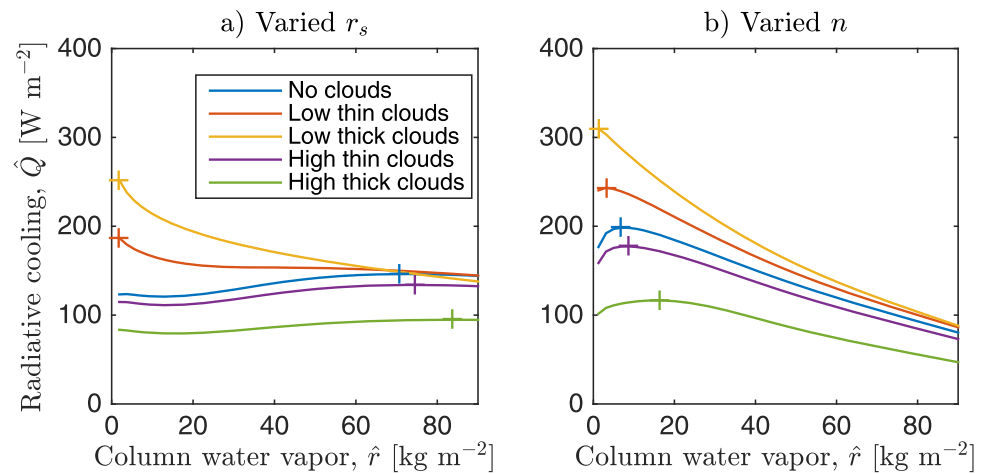
Figure 9. Dependence of total radiative cooling $\widehat{Q}$ on column water vapor $\widehat{r}$ in RRTMG calculations that include cloud layers, for (a) varied surface mixing ratio and (b) varied water vapor profile shape. The four different types of clouds correspond to those described in section 2.4 and Figure 7. The surface temperature is 300 K.

The existence of multiple ranges of column water vapor where MRCI is satisfied may be relevant to the finding of self-aggregation in cloud-resolving simulations in snowball earth-like conditions [*Abbot*, 2014].

As in the case of gray radiative transfer, low clouds increase the MRCI growth rate, and high clouds decrease the MRCI growth rate (Figure 9). Shortwave cloud effects are included in these calculations, but do not alter the conclusions reached in section 2.4. Clouds most strongly influence our findings for dry profiles with varied r_s, where water vapor perturbations that would be stable in clear-sky conditions are unstable in the presence of thick low clouds.

Overall, the calculations shown here suggest that clear-sky longwave MRCI may be satisfied in the real atmosphere, but is likely sensitive to whether real variability of water vapor profiles looks more like the case of varied shape (varied n), or that of varied surface mixing ratio (varied r_s).

4. Observations

4.1. Method
We investigate the following question: does the observed variability of Tropical water vapor lead to clear-sky MRCI? For a given meteorological station and a given month of the year, we proceed in two steps. First, we retrieve 20 consecutive years of bi-daily soundings (from the University of Wyoming archive, at www.weather.uwyo.edu/upperair/sounding.html). We eliminate the soundings that have less than 10 data points, as well as those which do not have complete data between 950 hPa and 100 hPa. The locations of the 12 stations are chosen in three distinct tropical zones, summarized in Table 1.

For each station, we average the temperature soundings to obtain the mean profile $T_{av}(p)$, and we examine the variability of the relative humidity in the soundings $RH(p)$. Relative humidity is defined as the ratio of the water vapor partial pressure $e(p)$ to its saturation value $e_{sat}(T, p)$:

$$RH(p) \overset{def}{=} \frac{e(p)}{e_{sat}(T, p)} \approx \frac{r(p)}{r_{sat}(T, p)}. \tag{23}$$

We have introduced the water vapor saturation mixing ratio $r_{sat}(p)$, which is the mixing ratio above which water vapor condenses. To capture the essence of this variability, we generate three soundings for each station, based on column relative humidity $\mathcal{H}$:

$$\mathcal{H} \overset{def}{=} \frac{\widehat{r}}{\widehat{r}_{sat}}, \tag{24}$$

which is the ratio of the total column water vapor to the column-integrated saturation mixing ratio. The three soundings are:

Table 1. Locations of the Stations Used in Sounding Analysis[a]

| Region | Location | Station ID | Number of Soundings | | | |
			Jan	Apr	Jul	Oct
Caribbean	International airport of Barbados, Barbados	78954 TBPB	456	457	657	699
Caribbean	San Juan, Puerto Rico (US)	78526 TJSJ	1127	1105	1120	1133
Caribbean	Santo Domingo, Dominican Republic	78486 MDSD	158	190	272	301
W. Pacific	Pohnpei, Federated States of Micronesia	91348 PTPN	1150	1079	1116	1087
W. Pacific	Chuuk Lagoon, Federated States of Micronesia	91334 PTKK	1141	1116	1080	1077
W. Pacific	Guam International Airport, Guam (US)	91212 PGAC	885	947	850	781
W. Pacific	Yap Main Islands, Federated States of Micronesia	91413 PTYA	1074	1085	1072	1010
W. Pacific	Koror Island, Palau	91408 PTRO	1068	1123	1214	1127
Amazon	Manaus International Airport, Brazil	82332 SBMN	600	592	620	621
Amazon	Sao Gabriel da Cachoeira, Brazil	82107	72	72	75	58
Amazon	Santarem, Brazil	82244	157	103	111	179
Amazon	Tabatinga, Brazil	82411	94	61	85	58

[a]Number of soundings used for each season indicated in the rightmost columns.

1. Average: The ensemble average of the relative humidity profile: $RH_{av}(p)$.
2. Moist: The ensemble average of relative humidity from the moistest profiles: $RH_{moist}(p)$, defined as those with column relative humidity (24) one standard deviation or more above the mean ($+1\sigma$).
3. Dry: The ensemble average of relative humidity from the driest profiles: $RH_{dry}(p)$, defined as those with column relative humidity (24) one standard deviation or more below the mean (-1σ).

We then use the longwave and shortwave packages from the RRTMG to estimate the radiative fluxes for each case. The input to RRTMG includes:

1. A standard pressure profile, with sixty levels spaced by 20.5hPa from 1000hPa to 85hPa and with a decreasing spacing above 85hPa.
2. The interpolated mean temperature profile $T_{av}(p)$. We find that the temperature in profiles corresponding to RH_{av}, RH_{dry} and RH_{moist} varies by only a few tenths of a degree, and leads to only small changes in the perturbation radiative cooling (of order a few W m^{-2}). Together with our focus on radiative perturbations caused solely by water vapor variability, this justifies the use of a single average temperature profile for all three cases.
3. The water vapor mixing ratio in the average, moist, and dry cases, obtained from the interpolated relative humidity levels, the exact version of definition (23) and Bolton's formula for the saturation water vapor partial pressure [*Bolton*, 1980].
4. Carbon dioxide with a constant mixing ratio of 4.0×10^{-4}, is the only long-lived greenhouse gas. Note that the lack of ozone decreases stratospheric shortwave absorption, resulting in an overestimate of tropospheric shortwave heating, and its sensitivity to $\hat{r}$.
5. A solar zenith angle of $\arccos(\pi/4)$rad, the equatorial equinox value.

Finally, we obtain the net longwave and shortwave radiative fluxes at all pressure levels (the shortwave fluxes must be multiplied by $\frac{4}{\pi^2}$ to account for the diurnal cycle and the zenith angle). We then compute the total radiative cooling by subtracting the surface net longwave flux from the top of the atmosphere net longwave flux, following definition (17). To summarize, this method allows us to go from environmental variability of relative humidity ($RH_{av}, RH_{moist}, RH_{dry}$) to environmental variability of clear-sky atmospheric radiative cooling ($\hat{Q}_{av}, \hat{Q}_{moist}, \hat{Q}_{dry}$), assuming that the temperature profile is unchanged and equal to its mean value $T_{av}(p)$.

4.2. A Case Study: Chuuk Lagoon

We focus on Chuuk Lagoon (Federated States of Micronesia, station 91334 PTKK); the computed mixing ratio profile used for the RRTMG input, the profile relative humidity, and its net upward longwave and shortwave fluxes are plotted in Figure 10. We expect this station to be a good candidate for MRCI because column water vapor is high (on average $\hat{r} \approx 43$ kg m^{-2}), and because the variability of water vapor is small near the surface but much larger in the mid to upper troposphere (Figures 10a and 10b). Indeed, we find MRCI at this station: $\hat{Q}_{moist} < \hat{Q}_{av} < \hat{Q}_{dry}$ (Figures 10a and 10b); this confirms that in the moist Tropics, increasing water vapor can lead to less longwave radiative cooling. Furthermore, as with section 2.3, the shortwave radiative heating increases with column water vapor. Total radiative cooling $\hat{Q}$ thus decreases faster with column water vapor
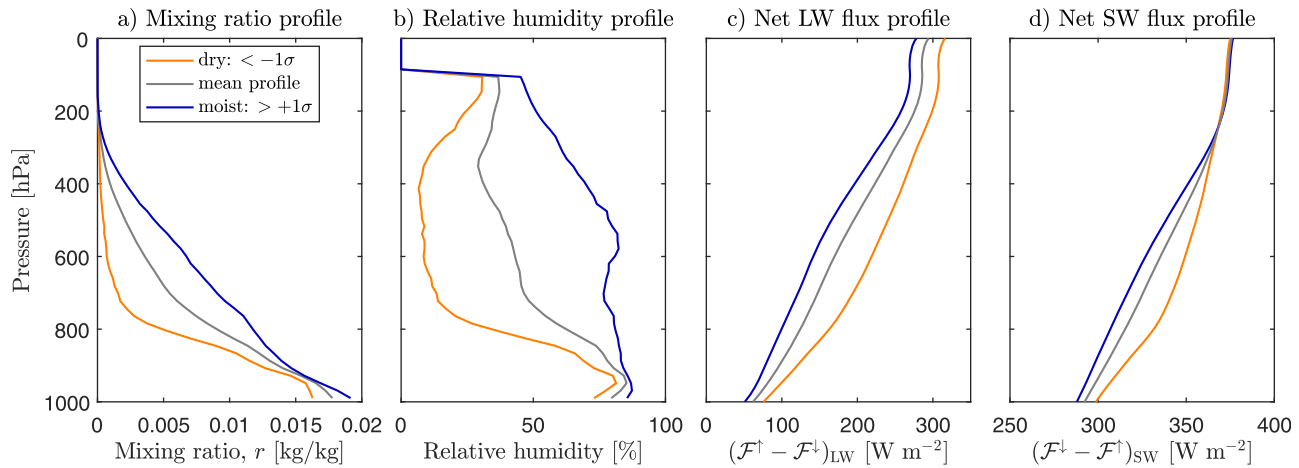
Figure 10. For Chuuk Lagoon station, profiles for average (gray line), $+1\sigma$ (blue line) and -1σ (orange line) conditions: (a) Computed mixing ratio profiles used for the RRTMG input, (b) relative humidity profiles, (c) net upward longwave radiative flux, (d) net downward shortwave radiative flux. Longwave radiative cooling values $\widehat{Q}_L$ are respectively 241 (dry: $< -1\sigma$), 233 (average), and 227 (moist: $> +1\sigma$) W m^{-2}. The shortwave radiative heating values $-\widehat{Q}_S$ are respectively 76 (dry: $< -1\sigma$), 84 (average), and 89 (moist: $> +1\sigma$) W m^{-2}.

than the longwave radiative cooling alone, which confirms that the shortwave heating enhances MRCI in the Tropics. From equation (6), we can estimate the clear-sky MRCI growth rate λ:

$$\lambda_- \approx \frac{\widehat{Q}_{dry} - \widehat{Q}_{av}}{\widehat{r}_{av} - \widehat{r}_{dry}} \qquad (25)$$

$$\lambda_+ \approx \frac{\widehat{Q}_{av} - \widehat{Q}_{moist}}{\widehat{r}_{moist} - \widehat{r}_{av}}. \qquad (26)$$

For Chuuk Lagoon, we obtain growth rates of $\lambda_{-,+} = (1.6, 1.2)$month^{-1}, suggesting potential growth of moisture anomalies via MRCI with a time scale of several weeks. Given this one unstable case study, we ask: Are most tropical locations unstable to MRCI, and what are their typical MRCI growth rates?

4.3. MRCI Growth Rates in the Tropics

In this section, we present 48 case studies, where 20 consecutive years of bi-daily soundings were retrieved for each case study. We study 12 different stations spread over the Tropics (see section 4.1), for 4 different months of the year (January, April, July, and October). For all cases studied, the longwave and the total radiative cooling decrease with column water vapor ($\widehat{Q}_{dry} > \widehat{Q}_{av} > \widehat{Q}_{moist}$). Thus, observed variability of water vapor is consistent with presence of MRCI at all these tropical locations. We estimate the growth rates at each of these locations from equation (26), and plot them as a function of column water vapor on Figure 11. Looking at the clear-sky longwave growth rates (Figure 11a), we notice that most of the longwave growth rates are below 1 month. We also see clear geographical groups: the Caribbean soundings (blue squares with red borders) are drier than the Western Pacific ones (blue stars), which are drier than the Amazonian ones (green circles with yellow borders). Some of the highest longwave growth rates occur for the moist soundings, but the variability is too large to discern a clear trend. We have also not found a clear seasonality in MRCI growth rates, although the latter tend to be larger during the wet season at a given location.

Looking at the total clear-sky growth rates (Figure 11b), we see that the growth rates have increased and are now all above 1 month. Additionally, the shortwave feedback is strongest for the driest locations. This is due to diminishing sensitivity of shortwave absorption by water vapor as column water vapor increases, as the most strongly absorbing bands saturate (see also Figure 8 of section 3). A stronger shortwave feedback in dry regions is also predicted by the gray-gas model as absorption saturates throughout the shortwave (equation (21) of section 2.3).

In conclusion, the clear-sky MRCI is common across the tropics but has fairly low growth rates $\lesssim 1$ month, but the shortwave feedback roughly doubles typical growth rates, leading to values that are more characteristic of tropical intraseasonal disturbances. If the same method is applied to midlatitude, or polar
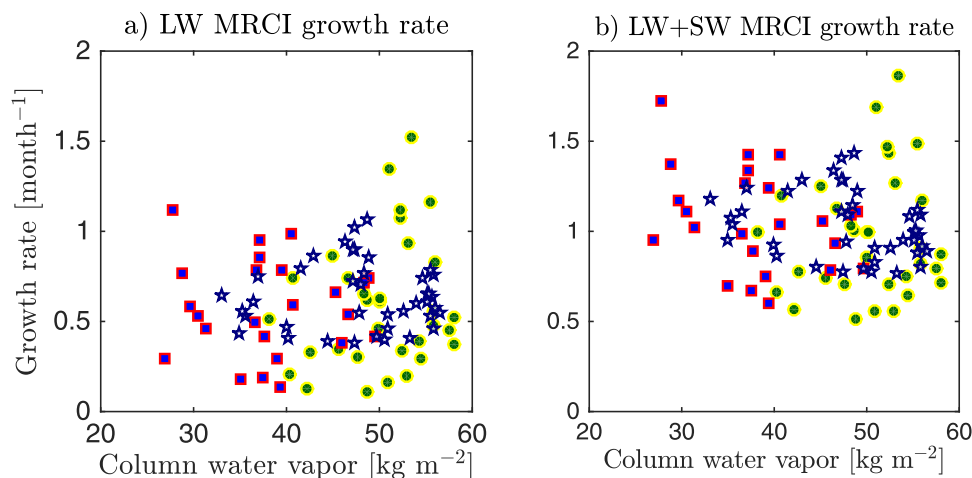
Figure 11. Observed MRCI growth rates based on (a) slope of clear-sky longwave cooling versus column water vapor and (b) slope of clear-sky longwave plus shortwave cooling versus column water vapor, for the Caribbean stations (blue squares with red borders) West Pacific stations (blue stars) and Amazonian stations (green circles with yellow borders).

soundings, we find that the clear-sky longwave effects are not sufficient to destabilize the atmosphere ($\widehat{Q}_{dry} < \widehat{Q}_{av} < \widehat{Q}_{moist}$), suggesting that MRCI is unique to the Tropics. This finding owes to both the latitudinally varying shape of water vapor perturbations—varied-r_s perturbations are more common outside the Tropics—as well as to lower climatological $\widehat{r}$ values outside the tropics. Furthermore, the structural model assumption of weak temperature gradients, which implies that variations in column $\widehat{MSE}$ are dominated by variations in $L_v\widehat{r}$, is clearly invalid outside the Tropics.

5. Conclusion

We have defined a moisture-radiative cooling instability (MRCI) criterion for the tropical atmosphere; MRCI is satisfied if total column radiative cooling decreases with increasing column water vapor. When the atmosphere is very moist, adding water vapor reduces atmospheric longwave cooling. With a smaller cooling rate, the tropical atmosphere gains energy, mainly in the form of latent heat, which increases its moisture content. In this very moist atmosphere, a dry moisture perturbation will also amplify through the opposite mechanism. In the shortwave, adding water vapor to a column increases the absorption of solar radiation, further energizing the column. Translating MRCI into an actual instability of moisture perturbations relies fundamentally on the assumption of weak temperature gradients in the tropical atmosphere, so that heating anomalies translate to vertical motion anomalies that moisten or dry the atmosphere by large-scale water vapor convergence or divergence.

We have used the gray approximation for much of the paper for illustrative purposes, but we have also shown that MRCI operates with real-gas radiative transfer calculations. Both the gray-gas and real-gas approximations highlight the importance of the vertical structure of water vapor perturbations for MRCI. If moist and dry anomalies occur dominantly in the mid and upper troposphere, MRCI is satisfied for a larger range of column water vapor values, and its growth rates are larger. We have also shown that static clouds, especially low and thick clouds, can expand the range of column water vapor values for which MRCI is satisfied and lead to larger growth rates.

Analysis of observational soundings with a radiative transfer model suggests that MRCI is common across the real Tropics, and has growth rates of ∼1 month. MRCI is favored in the Tropics because column water vapor values are high, and because moisture anomalies occur preferentially in the mid and upper troposphere; the boundary layer and surface humidity do not vary much.

Our key criterion for MRCI is that radiative cooling decrease with column water vapor. This criterion differs from *Emanuel et al.* [2014] in several ways:

1. It is a bulk, vertically integrated criterion, which is simple to test against observations and model outputs.

2. The occurrence of MRCI does not explicitly rely on the vertical structure of the convective fluxes; however, its growth rate relies on the vertical structure of water vapor, and convection is important for vertical redistribution of water vapor.

3. It is valid in the optically thin and the optically thick limits, and can be easily used at any surface temperature and column water vapor, particularly if real-gas radiative transfer models are used.

Our results show mixed agreement with the studies of *Wing and Emanuel* [2014] and *Emanuel et al.* [2014]. In agreement with previous work, our results with the gray approximation do suggest a threshold in RCE column water vapor below which RCE is stable. The threshold, however, is sensitive to both the basic-state clouds and the vertical structure of water vapor perturbation. Note that *Emanuel et al.* [2014] suggested a temperature-based instability threshold of ∼35–40°C, but as they used radiative transfer calculations with varied r_s to make this deduction, their temperature limit may be considerably too high. Additionally, real-gas radiative modeling suggests that multiple thresholds may exist in certain cases, as different wavelengths in the infrared become opaque at different column water vapor values. Thus, although the notion of a single temperature threshold simplifies the conceptual understanding of MRCI, it is not accurate for real-gas radiation, especially when clouds and shortwave feedbacks are included.

When MRCI is satisfied, an anomalously moist atmospheric column induces a large-scale ascent and moisture convergence. The vertical structure of this circulation can play an important role in amplifying or damping the radiation-water vapor instability [e.g., *Muller and Bony*, 2015]. Furthermore, our idealized model of clouds shows how MRCI can be satisfied for dry atmospheres in the presence of low thick clouds, consistent with the results of *Coppin and Bony* [2015] at low temperatures. It is important to note that MRCI is defined at fixed surface temperature and surface fluxes, meaning that this instability is entirely separate from the wind induced surface heat exchange mechanism [*Emanuel*, 1987]. Studies of self-aggregation, however, have shown that radiation and surface flux feedbacks usually act in concert early in the process of aggregation, so MRCI may be amplified by feedbacks between column water vapor and surface turbulent fluxes [*Wing and Emanuel*, 2014; *Wing and Cronin*, 2016]. Note also that MRCI is defined at a fixed temperature profile, so there is no negative Planck feedback associated with increasing column water vapor; MRCI is not linked with the runaway greenhouse effect [*Ingersoll*, 1969; *Pujol and North*, 2002].

This work points to many open questions about self-aggregation and moisture-radiative cooling instability. Most pertinent to the work that we have shown here is the question: what determines the vertical structure of moisture perturbations? One approach to the problem would be to formulate the coupling between moisture, radiative cooling, and large-scale convergence of moisture as an eigenvalue problem, fixing the convective heating and moistening rates for simplicity. Preliminary investigation suggests that this is a rich problem, which may give intense nonnormal growth but no unstable normal modes, due to the tendency of radiative cooling anomalies to propagate downward [e.g., *Emanuel et al.*, 2014, Figure 4]. Our work also suggests that observation-based investigation of the correlation between cloud and moisture anomalies would be important to constrain the magnitude of MRCI growth rates in the real world. Finally, we note that MRCI may be relevant to the regulation of climates on other worlds, with "moisture" representing a general condensible greenhouse gas (e.g., methane on Titan)—and that MRCI is likely to be of particular importance on slowly rotating worlds with wide "tropics" in the habitable zone.

Appendix A: Analytical Form of the Longwave Radiative Fluxes

To compute the longwave radiative fluxes, the first step is to substitute the temperature as a function of the optical thickness (13) in the Schwarzschild equations (10) and (11), yielding:

$$\frac{d\mathcal{F}_\uparrow}{d\tau} = \mathcal{F}_\uparrow - \sigma T_s^4 \left(\frac{\tau}{\tau_s}\right)^\alpha, \tag{A1}$$

$$\frac{d\mathcal{F}_\downarrow}{d\tau} = -\mathcal{F}_\downarrow + \sigma T_s^4 \left(\frac{\tau}{\tau_s}\right)^\alpha. \tag{A2}$$

The boundary conditions in the longwave are:

- No downwelling flux at the top of the atmosphere: $\mathcal{F}_\downarrow(\tau=0)=0$.
- The surface radiates like a blackbody of temperature T_s: $\mathcal{F}_\uparrow(\tau=\tau_s)=\sigma T_s^4$.
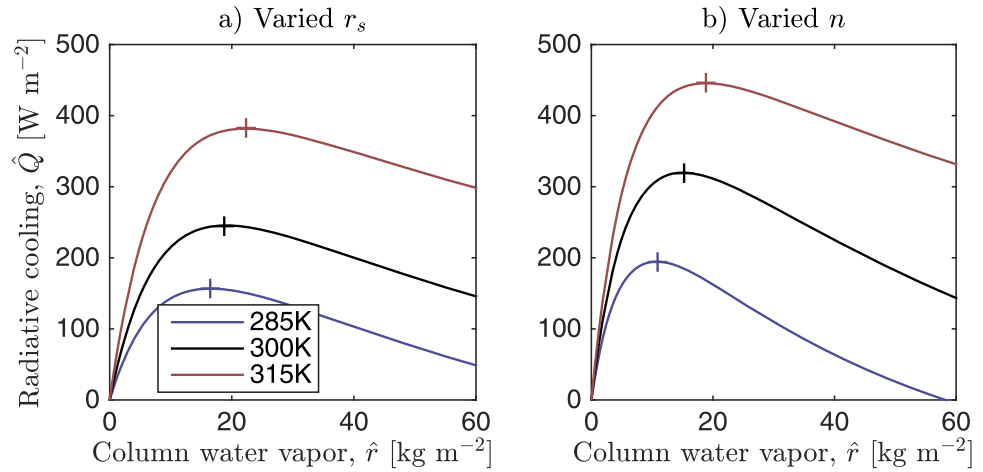
Figure B1. Total $\hat{Q}$ clear-sky radiative cooling as a function of column water vapor, (a) varying the surface mixing ratio at fixed shape, and (b) varying the water vapor profile shape at constant surface mixing ratio, for three different choices of surface temperature. Crosses show maxima of radiative cooling.

The fixed surface temperature T_s, the total optical thickness τ_s, and the exponent α are independent of τ. Thus, we can integrate equation (A1) from $\tau'=\tau$ to $\tau'=\tau_s$, and equation (A2) from $\tau'=0$ to $\tau'=\tau$:

$$\frac{\mathcal{F}_\uparrow(\tau)}{\sigma T_s^4} = e^{-(\tau_s-\tau)} + \int_\tau^{\tau_s} d\tau' \left(\frac{\tau'}{\tau_s}\right)^\alpha e^{-(\tau'-\tau)}, \tag{A3}$$

$$\frac{\mathcal{F}_\downarrow(\tau)}{\sigma T_s^4} = \int_0^\tau d\tau' \left(\frac{\tau'}{\tau_s}\right)^\alpha e^{-(\tau-\tau')}. \tag{A4}$$

The radiative fluxes (15), (16) and (17) can then be obtained from the upwelling and downwelling longwave fluxes (A.3) and (A.4).

Appendix B: Dependence of MRCI on Surface Temperature

MRCI is studied at fixed surface temperature $\overline{T_s}$, and its characteristics (e.g., its growth rate) depend directly and indirectly on $\overline{T_s}$. First, the moist adiabatic lapse rate Γ_m is a function of the atmospheric temperature, and decreases with warming [e.g., *Holton*, 1973]. Thus, the exponent α defined by (13) also decreases with increasing $\overline{T_s}$. Second, the RCE surface mixing ratio depends on the saturation mixing ratio at the surface, which exponentially increases with increasing $\overline{T_s}$.
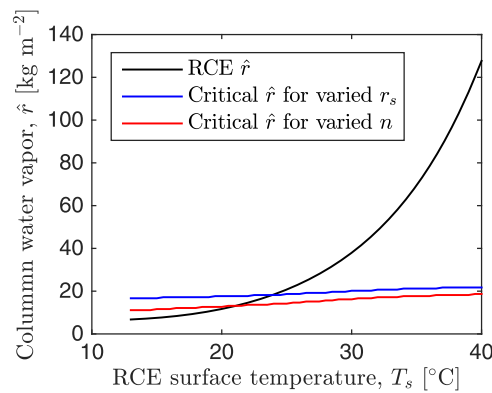

Figure B2. RCE column water vapor (black line) and critical column water vapor threshold $\widehat{r}_{crit}$, as a function of the surface temperature. On the left of the intersection point, RCE is stable. On the right of the intersection point, MRCI is satisfied. We obtain approximate surface temperature thresholds of 21°C for varied shape, and 24°C for varied surface mixing ratio. These values should be taken as illustrative rather than exact, and are sensitive to model assumptions.

We find that the critical threshold $\widehat{r}_{crit}$ for MRCI decreases with increasing surface temperature, and typical MRCI growth rates decrease with increasing surface temperature (Figure B1). Physically, the atmosphere has a smaller lapse rate for higher surface temperatures, leading to a smaller change in the effective upward emission temperature for a given change in emission height. Thus, the OLR decreases less for a given moistening of the atmosphere, raising $\widehat{r}_{crit}$ and decreasing the MRCI growth rate. Effects of varying r_s with temperature are more subtle, but we have found that an increase in the lapse rate Γ_m at constant r_s, as well as an increase in r_s at constant Γ_m, both lead to an increase in $\widehat{r}_{crit}$ and a decrease in growth rate.

In Figure B2, we check that $\widehat{r}_{crit}(T_s)$ increases slowly enough with temperature to still obtain a surface

temperature threshold $\overline{T_s}$ for MRCI, consistent with *Wing and Emanuel* [2014]. The typical RCE column water vapor profile as a function of $\overline{T_s}$ was numerically computed using the toy model of *Beucler and Emanuel* [2016]. Note that the temperature threshold is sensitive to the water vapor profile and the cloud cover. Furthermore, the notion of a single temperature threshold only applies for gray radiation, whereas we have seen in section 3 that real-gas radiation can exhibit multiple thresholds or none.

Appendix C: Cloudy Radiative Fluxes

In Figure 6, we defined a cloud by its optical thickness $\Delta\tau$ and its pressure level p_c, so that the atmospheric optical thickness is given by:

$$\frac{\tau}{\tau_s} = \begin{cases} (p/p_s)^{n+2} & \text{if } p \leq p_c \\ (p/p_s)^{n+2} + \Delta\tau/\tau_s & \text{if } p \geq p_c \end{cases}.$$ (C1)

By combining the temperature profile (9) to the cloudy optical thickness profile (C.1), we can express the temperature as a function of the optical thickness in the presence of a cloud:

$$\frac{T}{T_s} = \begin{cases} (\tau/\tau_s)^{\alpha/4} & \text{if } \tau \leq \tau_c \\ (T_c/T_s) & \text{if } \tau_c \leq \tau \leq \tau_c + \Delta\tau \\ [(\tau-\Delta\tau)/\tau_s]^{\alpha/4} & \text{if } \tau \geq \tau_c + \Delta\tau \end{cases}.$$

We have defined the optical thickness τ_c right above the cloud:

$$\tau_c \overset{\text{def}}{=} \tau_s \left(\frac{p_c}{p_s}\right)^{n+2},$$

so that the cloud can be found between τ_c and $\tau_c + \Delta\tau$ in optical thickness coordinates. The cloud has a constant temperature T_c, set by the moist adiabatic temperature at pressure level p_c:

$$T_c \overset{\text{def}}{=} T_s \left(\frac{p_c}{p_s}\right)^{\alpha_0/4},$$

where we have defined the introduced α_0, defined by:

$$\alpha_0 \overset{\text{def}}{=} (n+2)\alpha = \frac{4\Gamma_m R_d}{g},$$ (C2)

Integrating equations (A1) and (A2) in the presence of a cloud, between the ground at $\tau = \tau_s + \Delta\tau$ and the top of the atmosphere at $\tau = 0$, leads to the following total radiative cooling:

$$\frac{\widehat{Q}}{\sigma T_s^4} = \underbrace{-1}_{\text{Surface}\to\text{Atmosphere}} + \underbrace{e^{-(\tau_s+\Delta\tau)}}_{\text{Atmosphere}\to\text{Space}} - \underbrace{\frac{S}{\sigma T_s^4}(1-e^{-\varepsilon\tau_s})}_{\text{Shortwave absorption}}$$

$$+ \underbrace{\int_0^{\tau_c} d\tau' \left(\frac{\tau'}{\tau_s}\right)^\alpha \left(e^{-(\tau_s+\Delta\tau-\tau')} + e^{-\tau'}\right)}_{\text{Emission of atmosphere above cloud}} + \underbrace{\int_{\tau_c+\Delta\tau}^{\tau_s+\Delta\tau} d\tau' \left(\frac{\tau'-\Delta\tau}{\tau_s}\right)^\alpha \left(e^{-(\tau_s+\Delta\tau-\tau')} + e^{-\tau'}\right)}_{\text{Emission of atmosphere below cloud}}$$

$$+ \underbrace{2\left(\frac{T_c}{T_s}\right)^4 \sinh\left(\frac{\Delta\tau}{2}\right)\left(e^{-(\tau_c+\frac{\Delta\tau}{2})} + e^{-(\tau_s+\frac{\Delta\tau}{2}-\tau_c)}\right)}_{\text{Cloud emission}}.$$ (C3)

Note that we neglect the shortwave effects of the cloud entirely, using only clear-sky shortwave heating. In reality thick clouds reflect much of the incoming shortwave radiation back to space, which is then partially absorbed by the atmosphere above the cloud. This means that our model overestimates the shortwave radiative heating below the cloud, and underestimates the shortwave radiative heating above the cloud.

Appendix D: Growth Rates of MRCI

According to equation (6), the growth rate of the instability (in units s^{-1}) is given by:

$$\overline{\left(\frac{\dot{\widehat{r}}}{\partial \widehat{r}}\right)} = -\frac{1}{L_v}\overline{\frac{\partial \widehat{Q}}{\partial \widehat{r}}}, \tag{D1}$$

where the radiative cooling is given by equation (17) as a function of T_s, τ_s and α. We always study MRCI at fixed temperature T_s. First, we compute the growth rate at fixed shape (i.e., fixed exponent α); according to the chain rule:

$$\left(\frac{\dot{\widehat{r}}}{\partial \widehat{r}}\right)_\alpha = -\frac{1}{L_v}\left(\frac{\partial \widehat{Q}}{\partial \widehat{r}}\right)_\alpha = -\frac{1}{L_v}\left(\frac{\partial \tau_s}{\partial \widehat{r}}\right)_\alpha\left(\frac{\partial \widehat{Q}}{\partial \tau_s}\right)_\alpha. \tag{D2}$$

By combining the expression for column water vapor (18) with the one for total optical thickness (14), we can express the total optical thickness as a function of column water vapor and fixed parameters:

$$\tau_s = Dk\frac{n+1}{n+2}\widehat{r} \;\Rightarrow\; \left(\frac{\partial \tau_s}{\partial \widehat{r}}\right)_\alpha = Dk\frac{n+1}{n+2}. \tag{D3}$$

We finally combine equations (D2), (D3), and use the Leibniz rule to compute the growth rate at fixed shape:

$$\begin{aligned}\frac{L_v}{kD\sigma T_s^4}\frac{n+2}{n+1}\left(\frac{\dot{\widehat{r}}}{\partial \widehat{r}}\right)_\alpha &= -\left(\frac{\partial}{\partial \tau_s}\right)_\alpha\frac{\widehat{Q}}{\sigma T_s^4} \\ &= -1 + \int_0^{\tau_s} d\tau'\left(\frac{\tau'}{\tau_s}\right)^\alpha\left[\left(1+\frac{\alpha}{\tau_s}\right)e^{-(\tau_s-\tau')}+\frac{\alpha e^{-\tau'}}{\tau_s}\right]\end{aligned}. \tag{D4}$$

Computing the growth rate at fixed surface mixing ratio (i.e., fixed r_s) is more involved, as both τ_s and α now vary with $\widehat{r}$; according to the chain rule:

$$\left(\frac{\dot{\widehat{r}}}{\partial \widehat{r}}\right)_{r_s} = -\frac{1}{L_v}\left[\left(\frac{\partial \tau_s}{\partial \widehat{r}}\right)_{r_s}\left(\frac{\partial \widehat{Q}}{\partial \tau_s}\right)_\alpha + \left(\frac{\partial \alpha}{\partial \widehat{r}}\right)_{r_s}\left(\frac{\partial \widehat{Q}}{\partial \alpha}\right)_{\tau_s}\right]. \tag{D5}$$

We now need to relate the exponent α to column water vapor $\widehat{r}$ and fixed parameters, which can be done by combining the definition of α (13) to the expression (1) for column water vapor:

$$\alpha = \frac{\alpha_0\widehat{r}}{\widehat{r}_s+\widehat{r}} \;\Rightarrow\; \left(\frac{\partial \alpha}{\partial \widehat{r}}\right)_{r_s} = \frac{\alpha_0\widehat{r}_s}{(\widehat{r}_s+\widehat{r})^2}. \tag{D6}$$

We have introduced two fixed parameters: the coefficient α_0, defined by equation (C2), and the hypothetical value of the column water vapor if the mixing ratio was equal to r_s everywhere:

$$\widehat{r}_s \overset{\text{def}}{=} \frac{r_s p_s}{g}. \tag{D7}$$

Combining equations (14), (18) to the definitions (C.2) and (D.7), it is possible to express τ_s as a function of $\widehat{r}$ and fixed parameters:

$$\tau_s = \frac{kD\widehat{r}_s\widehat{r}}{\widehat{r}_s+\widehat{r}} \;\Rightarrow\; \left(\frac{\partial \tau_s}{\partial \widehat{r}}\right)_{r_s} = kD\left(\frac{\widehat{r}_s}{\widehat{r}_s+\widehat{r}}\right)^2. \tag{D8}$$

We finally combine equations (D5), (D6), (D8), and use the Leibniz rule to compute the growth rate at fixed surface mixing ratio:

$$\frac{L_v}{kD\sigma T_s^4}\left(\frac{\widehat{r}_s+\widehat{r}}{\widehat{r}_s}\right)^2\left(\frac{\partial\dot{\widehat{r}}}{\partial\widehat{r}}\right)_{r_s}=-\left[\left(\frac{\partial}{\partial\tau_s}\right)_\alpha+\frac{\alpha_0}{kD\widehat{r}_s}\left(\frac{\partial}{\partial\alpha}\right)_{\tau_s}\right]\frac{\widehat{Q}}{\sigma T_s^4}$$

$$=-1+\int_0^{\tau_s}d\tau'\left(\frac{\tau'}{\tau_s}\right)^\alpha\left[\left(1+\frac{\alpha}{\tau_s}\right)e^{-(\tau_s-\tau')}+\frac{\alpha e^{-\tau'}}{\tau_s}-\frac{\alpha_0\log\left(\frac{\tau'}{\tau_s}\right)}{kD\widehat{r}_s}\left(e^{-(\tau_s-\tau')}+e^{-\tau'}\right)\right].$$

(D9)

Appendix E: Two-Band Longwave Radiative Transfer

A two-band longwave radiative transfer model can be used to distinguish between wavelengths with strong absorption and those with weak absorption, and provides a much better representation of real-gas radiative transfer for water vapor than a single gray-gas absorption coefficient. We assume that the two bands contain fractional amounts of the longwave spectrum that do not vary with temperature, as in the windowed-gray model of *Weaver and Ramanathan* [1995]. For strongly absorbing wavelengths—corresponding roughly to both the pure rotational bands of water vapor at wavelengths $>15\,\mu$m, and the ro-vibrational complex centered at $6.3\,\mu$m—we use a large absorption coefficient $k_{LW,1}=1$ m^2 kg^{-1}. For weakly absorbing wavelengths—including the major spectral window with wavelength 8–15 μm and the less important window to the shortwave side of 5 μm—we use a much smaller absorption coefficient $k_{LW,2}=0.02$ m^2 kg^{-1}. As these spectral regions occupy roughly equal fractions of blackbody emission at $\sim$ 300 K, the two-band longwave fluxes are simply given by an average of the broadband flux in the strongly absorbing regions and the weakly absorbing ones. For example, the radiative cooling is given by:

$$\widehat{Q}_{L,\text{two-band}}=\frac{\widehat{Q}_{L,1}+\widehat{Q}_{L,2}}{2},$$

(E1)

where we have used the gray longwave radiative cooling $\widehat{Q}_L$ given by equation (17), with subscripts 1 and 2 indicating that $k_{LW,1}$ is used to calculate half of the radiative cooling, and $k_{LW,2}$ is used for the other half. The two-band SLW, OLR and radiative cooling as a function of column water vapor are depicted in Figure E1, and compare well with the real-gas radiative cooling rates (Figure 8). The strongly absorbing regions saturate very quickly, which explains the sharp decrease of the SLW for small values of the column water vapor (a few kg m^{-2}). In contrast, the weakly absorbing windows only saturate for a very large amount of column water vapor (larger than 100 kg m^{-2}, higher than values seen on Earth). As a consequence, the two-band model captures the occurrence of MRCI at varied shape (varied n), where the SLW decreases slowly enough with $\widehat{r}$ for the longwave radiative cooling $\widehat{Q}_L$ to decrease with $\widehat{r}$ as well.
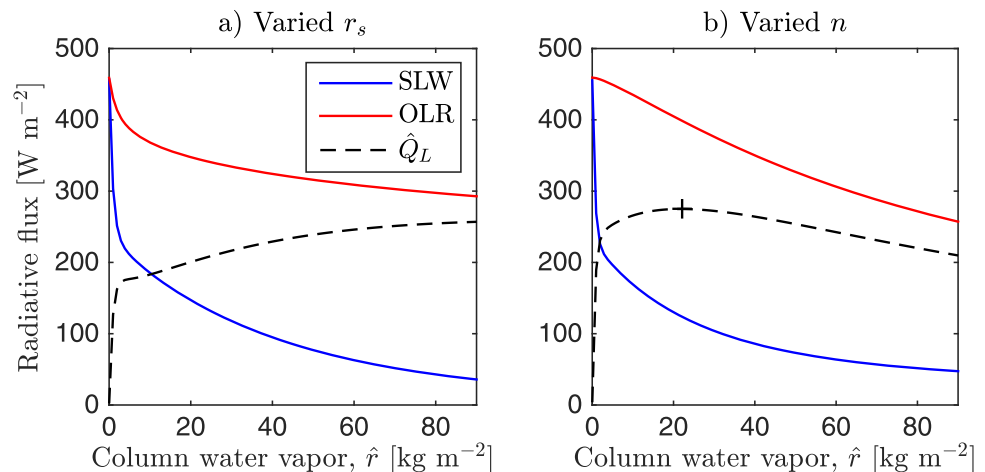

Figure E1. Two-band outgoing longwave radiation (OLR), surface net longwave radiation (SLW), and longwave clear-sky radiative cooling $\widehat{Q}_L$ as a function of column water vapor $\widehat{r}$, (a) varying the surface mixing ratio at fixed shape, and (b) varying the water vapor profile shape at constant surface mixing ratio. Crosses show maxima of radiative cooling.

References

Abbot, D. S. (2014), Resolved snowball earth clouds, *J. Clim.*, *27*, 4391–4402, doi:10.1175/JCLI-D-13-00738.1.

Allan, R. P., and B. J. Soden (2008), Atmospheric warming and the amplification of precipitation extremes, *Science*, *321*(5895), 14814, doi:10.1126/science.1160787.

Arakawa, A., and W. H. Schubert (1974), Interaction of a cumulus cloud ensemble with the large-scale environment, Part I, *J. Atmos. Sci.*, *31*, 674–701, doi:10.1175/1520-0469(1974)031<0674:IOACCE>2.0.CO;2.

Armstrong, B. H. (1968), Theory of the diffusivity factor for atmospheric radiation, *J. Quant. Spectrosc. Radiat. Transfer*, *8*, 1577–1599, doi:10.1016/0022-4073(68)90052-6.

Arnold, N. P., and D. A. Randall (2015), Global-scale convective aggregation: Implications for the Madden-Julian Oscillation, *J. Adv. Model. Earth Syst.*, *7*, 1499–1518, doi:10.1002/2015MS000498.

Beucler, T., and K. Emanuel (2016), Instabilities of radiative convective equilibrium with an interactive surface, paper presented at 32nd Conference on Hurricanes and Tropical Meteorology, Am. Meteorol. Soc., San Juan, Puerto Rico. [Available at https://ams.confex.com/ams/32Hurr/webprogram/Paper293918.html.]

Bolton, D. (1980), The computation of equivalent potential temperature, *Mon. Weather Rev.*, *108*(7), 1046–1053, doi:10.1175/1520-0493(1980)108<1046:TCOEPT>2.0.CO;2.

Bretherton, C. S., and M. F. Khairoutdinov (2015), Convective self-aggregation feedbacks in near-global cloud-resolving simulations of an aquaplanet, *J. Adv. Model. Earth Syst.*, *7*, 1765–1787, doi:10.1002/2015MS000499.

Bretherton, C. S., Blossey, P. N., and M. Khairoutdinov (2005), An Energy-Balance Analysis of Deep Convective Self-Aggregation above Uniform SST, *J. Atmos. Sci.*, *62*(12), 4273–4292, doi:10.1175/JAS3614.1.

Chandrasekhar, S. (1960), *Radiative Transfer*, 413 pp., Dover Publications, N. Y.

Coppin, D., and S. Bony (2015), Physical mechanisms controlling the initiation of convective self-aggregation in a general circulation model, *J. Adv. Model. Earth Syst.*, *7*, 2060–2078, doi:10.1002/2015MS000571.

Cormier, J. G., J. T. Hodges, and J. R. Drummond (2005), Infrared water vapor continuum absorption at atmospheric temperatures, *J. Chem. Phys.*, *122*, 114309, doi:10.1063/1.1862623.

Cronin, T. W. (2014), On the choice of average solar zenith angle, *J. Atmos. Sci.*, *71*(8), 2994–3003, doi:10.1175/JAS-D-13-0392.1.

Emanuel, K. A. (1987), An air-sea interaction model of intraseasonal oscillations in the tropics, *J. Atmos. Sci.*, *44*, 2324–2340, doi:10.1175/1520-0469(1987)044<2324:AASIMO>2.0.CO;2.

Emanuel, K. A. (1994), *Atmospheric Convection*, 580 pp., Oxford Univ. Press, N. Y. and Oxford, U. K.

Emanuel, K. A., A. A. Wing, and E. M. Vincent (2014), Radiative-convective instability, *J. Adv. Model. Earth Syst.*, *6*, 75–90, doi:10.1002/2013MS000270.

Harrop, B. E., and D. L. Hartmann (2015), The relationship between atmospheric convective radiative effect and net energy transport in the tropical warm pool, *J. Clim.*, *28*(21), 8620–8633, doi:10.1175/JCLI-D-15-0151.1.

Held, I. M., R. S.Hemler, and V. Ramaswamy (1993), Radiative-convective equilibrium with explicit two-dimensional moist convection, *J. Atmos. Sci.*, *50*, 3909–3927, doi:10.1175/1520-0469(1993)050<3909:RCEWET>2.0.CO;2.

Holloway, C. E., and S. J. Woolnough (2016), The sensitivity of convective aggregation to diabatic processes in idealized radiative-convective equilibrium simulations, *J. Adv. Model. Earth Syst.*, *8*, 166–195, doi:10.1002/2015MS000511.

Holton, J. R. (1973), An introduction to dynamic meteorology, *Am. J. Phys.*, 501–503, doi:10.1119/1.1987371.

Iacono, M. J., E. J. Mlawer, S. A. Clough and J.-J. Morcrette (2000), Impact of an improved longwave radiation model, RRTM. on the energy budget and thermodynamic properties of the NCAR community climate mode, CCM3, *J. Geophys. Res.*, *105*, 14,873–14,890.

Iacono, M. J., J. S. Delamere, E. J., Mlawer, M. W. Shephard, S. A. Clough, and W. D. Collins (2008), Radiative forcing by long-lived greenhouse gases: Calculations with the AER radiative transfer models, *J. Geophys, Res.*, *113*, D13103, doi:10.1029/2008JD009944.

Ingersoll, A. P. (1969), The runaway greenhouse: A history of water on venus, *J. Atmos. Sci.*, *26*(6), 1191–1198, doi:10.1175/1520-0469(1969)026<1191:TRGAHO>2.0.CO;2.

Inoue, K., and L. Back (2015a), Column-integrated moist static energy budget analysis on various time scales during TOGA COARE, *J. Atmos. Sci.*, *72*(5), 1856–1871, doi:10.1175/JAS-D-14-0249.1.

Inoue, K., and L. E. Back (2015b), Gross moist stability assessment during TOGA COARE: Various interpretations of gross moist stability, *J. Atmos. Sci.*, 1987, *72*, 4148–4166, doi:10.1175/JAS-D-15-0092.1.

Jeevanjee, N., and D. M. Romps (2013), Convective self-aggregation, cold pools, and domain size, *Geophys. Res. Lett.*, *40*, 994–998, doi:10.1002/grl.50204.

Khairoutdinov, M. F., and K. A. Emanuel (2013), Rotating radiative-convective equilibrium simulated by a cloud-resolving model, *J. Adv. Model. Earth Syst.*, *5*, 816–825, doi:10.1002/2013MS000253.

Liou, K. (2002), An Introduction to Aradiation, vol. 84, Academic press, Cambridge, Mass.

Manabe, S., and R. F. Strickler (1964), Thermal equilibrium of the atmosphere with a convective adjustment, *J. Atmos. Sci.*, *21*, 361–385, doi:10.1175/1520-0469(1964)021<0361:TEOTAW>2.0.CO;2.

Mlawer, E.J., S.J. Taubman, P.D. Brown, M.J. Iacono and S. A. Clough (1997), RRTMG, a validated correlated-k model for the longwave, *J. Geophys. Res.*, *102*, 16,663–16,682.

Muller, C., and S. Bony (2015), What favors convective aggregation and why?, *Geophys. Res. Lett.*, *42*, 5626–5634, doi:10.1002/2015GL064260.

Neelin, J. D., and I. M. Held (1987), Modeling tropical convergence based on the moist static energy budget, *Mon. Weather Rev.*, *115*, 3–12, doi:10.1175/1520-0493(1987)115<0003:MTCBOT>2.0.CO;2.

Nolan, D. S., E. D. Rappin, and K. A. Emanuel (2007), Tropical cyclogenesis sensitivity to environmental parameters in radiative-convective equilibrium, *Q. J. R. Meteorol. Soc.*, *133*, 2085–2107, doi:10.1002/qj.170.

Pujol, T., and G. R. North (2002), Runaway greenhouse effect in a semigray radiative convective model, *J. Atmos. Sci.*, *59*(1967), 2801–2810, doi:10.1175/1520-0469(2002)059<2801:RGEIAS>2.0.CO;2.

Ramanathan, V., and J. A. Coakley Jr. (1978), Climate modeling through radiative-convective models, *Rev. Geophys.*, *16*, 465–489, doi:10.1029/RG016i004p00465.

Robinson, T. D., and D. C. Catling (2012), An analytic radiative-convective model for planetary atmospheres, *Astrophys. J.*, *757*(1), 104, doi:10.1088/0004-637X/757/1/104.

Rodgers, C. D., and C. D. Walshaw (1966), The computation of infra-red cooling rate in planetary atmospheres, *Q. J. R. Meteorol. Soc.*, *92*, 67–92, doi:10.1002/qj.49709239107.

Sessions, S. L., M. J. Herman, and S. Senti (2015), Convective response to changes in the thermodynamic environment in idealized weak temperature gradient simulations, *J. Adv. Model. Earth Syst.*, *7*, 712–738, doi:10.1002/2015MS000446.

Sobel, A. H., J. Nilsson, and L. M. Polvani (2001), The weak temperature gradient approximation and balanced tropical moisture waves, *J. Atmos. Sci.*, *58*, 3650–3665, doi:10.1175/1520-0469(2001)058 <3650:TWTGAA >2.0.CO;2.

Sobel, A. H., G. Bellon, and J. Bacmeister (2007), Multiple equilibria in a single-column model of the tropical atmosphere, *Geophys. Res. Lett.*, *34*, L22804, doi:10.1029/2007GL031320.

Takahashi, K. (2009), Radiative constraints on the hydrological cycle in an idealized radiative convective equilibrium model, *J. Atmos. Sci.*, *66*(1), 7791, doi10.1175/2008JAS2797.1.

Tompkins, A. M. (2001), Organization of tropical convection in low vertical wind shears: The role of water vapor, *J. Atmos. Sci.*, *58*, 529–545, doi:10.1175/1520-0469(2001)058 <0529:OOTCIL >2.0.CO;2.

Weaver, C. P., and V. Ramanathan (1995), Deductions from a simple climate model: Factors governing surface temperature and atmospheric thermal structure, *J. Geophys. Res.*, doi:10.1029/95JD00770.

Wing, A. A., and T. W. Cronin (2016), Self-aggregation of convection in long channel geometry, *Q. J. R. Meteorol. Soc.*, *142*, 1–15, doi:10.1002/qj.2628.

Wing, A. A., and K. A. Emanuel (2014), Physical mechanisms controlling self-aggregation of convection in idealized numerical modeling simulations, *J. Adv. Model. Earth Syst.*, *6*, 59–74, doi:10.1002/2013MS000269.

Yu, J.-Y., C. Chou, and J. D. Neelin (1998), Estimating the gross moist stability of the tropical atmosphere, *J. Atmos. Sci.*, *55*, 1354–1372, doi:10.1175/1520-0469(1998)055 <1354:ETGMSO >2.0.CO;2.